The influence of packing structure and interparticle forces on ultrasound transmission in granular media

Chongpu Zhai[a] (ID), Eric B. Herbold[b] (ID), and Ryan C. Hurley[a,c,1] (ID)

[a]Hopkins Extreme Materials Institute, Johns Hopkins University, Baltimore, MD 21218; [b]Atmospheric, Earth, & Energy Division, Lawrence Livermore National Laboratory, Livermore, CA 94550; and [c]Department of Mechanical Engineering, Johns Hopkins University, Baltimore, MD 21218

Ultrasound propagation through externally stressed, disordered granular materials was experimentally and numerically investigated. Experiments employed piezoelectric transducers to excite and detect longitudinal ultrasound waves of various frequencies traveling through randomly packed sapphire spheres subjected to uniaxial compression. The experiments featured in situ X-ray tomography and diffraction measurements of contact fabric, particle kinematics, average per-particle stress tensors, and interparticle forces. The experimentally measured packing configuration and inferred interparticle forces at different sample stresses were used to construct spring networks characterized by Hessian and damping matrices. The ultrasound responses of these network were simulated to investigate the origins of wave velocity, acoustic paths, dispersion, and attenuation. Results revealed that both packing structure and interparticle force heterogeneity played an important role in controlling wave velocity and dispersion, while packing structure alone quantitatively explained most of the observed wave attenuation. This research provides insight into time- and frequency-domain features of wave propagation in randomly packed granular materials, shedding light on the fundamental mechanisms controlling wave velocities, dispersion, and attenuation in such systems.

granular materials | X-ray imaging | X-ray diffraction | ultrasound waves | interparticle forces

Stress wave propagation through granular media is important for detecting the magnitude of seismic events, locating oil and gas reservoirs, designing acoustic insulation and absorption materials, and designing materials for wave redirection (1–5). Granular materials form disordered packing structures and feature heterogeneous interparticle forces controlled by nonlinear contact laws (6–10). Ultrasound waves necessarily propagate through these interparticle contacts, making the prediction of wave behavior a highly nonlinear problem (11). Extensive research has been conducted using mathematical, numerical, and experimental tools to elucidate ultrasound wave behavior in granular materials in both the time and frequency domains. Some phenomena that have previously been studied include stress-dependent velocity scaling (8, 12), frequency filtering (8, 13, 14), wave dispersion (15–18), band gaps (8, 13, 19), rotational waves (17, 20–22), wave focusing (23), and wave scattering (20, 21, 24, 25).

In the time domain, the sound velocity of waves traveling through granular media has been found to follow a power-law relationship with respect to the applied pressure with an exponent varying from 1/4 to 1/6 for one-dimensional (1D) chains (8, 13, 26) and two-dimensional (2D) (27) and three-dimensional (3D) ordered (15, 16) sphere packing. Here, the exponent value of 1/6 corresponds to theoretical predictions of Hertzian contact and has been confirmed in solitary wave propagation experiments on 1D chains of spherical particles (8). The pressure-induced transition of power-law exponent ranging from 1/4 to 1/6 has also been observed not only for randomly packed spheres (12, 28, 29) but also, for natural geomaterials, including dry and water-saturated soils and sands, under both preconsolidation and overconsolidation (28, 30–33). This transition has been qualitatively attributed to the deformation of interparticle asperities (28), force chain arrangements (27, 28, 33), stress heterogeneity (32, 34), packing reorganization (12, 16, 29), nonspherical contact geometries (27, 32), wave modes (such as compressional and shear wave), and wave amplitudes (12, 32, 33, 35). However, a study quantitatively linking packing structure disorder and contact force heterogeneity to wave velocity and velocity scaling in 3D disordered granular materials has not yet been performed.

In the frequency domain, granular materials have been found to feature dispersion: waves propagate at different velocities depending on their wavelength (or frequency) and the material's particle size (24, 25). The acoustic signal measured through a disordered granular medium can be decomposed into coherent and incoherent parts. The coherent portion of the signal is the leading portion that represents the average of many measurements and provides a link to elastic properties and coordination number (16, 25, 36). The incoherent portion of the signal is the trailing portion that diminishes in magnitude when responses are averaged over an ensemble of the measured signals through the same packing configuration (16, 37). Theoretical calculations based on granular crystals that accounted for force balance and included Cosserat effects (17, 38) were able to provide reasonable predictions of wave dispersion for coherent waves in ordered granular materials. The differences between predictions and measurements were ascribed to nonlinearity of contacts and structural disorder. Unlike the propagation of plane waves

Significance

Structure-property relations of granular materials are governed by the arrangement of particles and the chains of forces between them. These relations enable design of wave damping materials and nondestructive testing technologies. Wave transmission in granular materials has been extensively studied and demonstrates rich features: power-law velocity scaling, dispersion, and attenuation. However, the precise roles of particle arrangements and force chains on these features remain topics of continued research interest. Here, we employ X-ray measurements and analyses to show that velocity scaling and dispersion arise from both particle arrangements and force chains, while attenuation arises mainly from particle arrangements.

in 1D chains and 2D and 3D granular crystals, the transmitted ultrasound signals for 3D disorder granular systems arise from a superposition of the signals traveling through different paths in this heterogeneous medium (23, 27, 39). Even small amounts of structural disorder can dramatically influence wave propagation, causing departures from theoretical force-dependent velocity scaling, dispersion, and attenuation (12, 16, 40, 41). Quantifying the influence of both structural disorder and force heterogeneity on dispersion may enhance the usefulness of using dispersion as a nondestructive probe of the state of a granular medium.

Both experiments and numerical simulations for ultrasound propagation have shown that coherent waves (including compressional, shear, and rotational waves) decay in amplitude with propagation distance. Frictional contact loss, viscoelastic/viscous contact dissipation, wave scattering, and material damping have been assumed to be responsible for wave attenuation (25, 35, 42, 43). Local contact damping has been incorporated in discrete element simulations (18, 35, 44–46), enabling analysis of the energy dissipation during wave propagation. Additionally, a stiffness matrix incorporating all particle contacts of a granular packing has been used to build a lattice-based model to examine the wave attenuation and scattering for 2D granular systems (20, 21, 47). However, limited experimental data are available to highlight the quantitative roles of packing disorder and force heterogeneity on wave attenuation in 3D.

The primary objective of this paper is to quantitatively investigate the relative influence of packing structure disorder and interparticle force heterogeneity on ultrasound wave velocity, dispersion, and attenuation in a disordered granular material. To achieve this, we combined in situ X-ray computed tomography (XRCT), three-dimensional X-ray diffraction (3DXRD), and ultrasound wave measurements during uniaxial compres-sion of a 3D disordered granular material in a unique loading frame (9, 10, 48). To evaluate the relative roles of packing structure and interparticle forces on wave behavior, we compared measurements of velocity, dispersion, and attenuation with simulations having contact networks controlled by measured interparticle forces and contact networks having uniform interparticle stiffness (equivalent to uniform forces). We further compared predictions with those made on isotropically loaded granular crystals to isolate the roles of packing structure disorder. Our results revealed that both packing structure and interparticle forces play important roles in controlling coherent wave velocities, velocity scaling, and dispersion, while packing structure alone can explain the majority of the observed wave attenuation.

Results and Discussion

Wave Velocity. The acoustic velocities of the coherent portions of ultrasound waves transmitted through a random packing of sapphire spheres under increasing normal compression were computed using cross-correlation analyses (*Materials and Methods* and *SI Appendix*, section 1C) and are presented in Fig. 1A. The measured acoustic velocity across load steps was found to follow a power-law dependence on the average vertical sample stress, $v \propto (\sigma_{zz}^s)^\alpha$, with exponents α of approximately 0.22 and 0.20 for input Gaussian bursts centered at 0.4 and 0.8 MHz, respectively. For the case of 0.4 MHz, the exponent was found to be close to 0.24 for load steps 2 to 6 and 0.21 for load steps 7 to 11, showing a decreasing trend as load increases. The exponents fell within the range of $\frac{1}{6}$ and $\frac{1}{4}$, comparable with reported empirical and semiempirical relationships in previous experiments and numerical simulations (8, 16, 24).

To simulate wave propagation through the packing at each load step, systems of equations were constructed for a spring network representing the experimentally measured structural
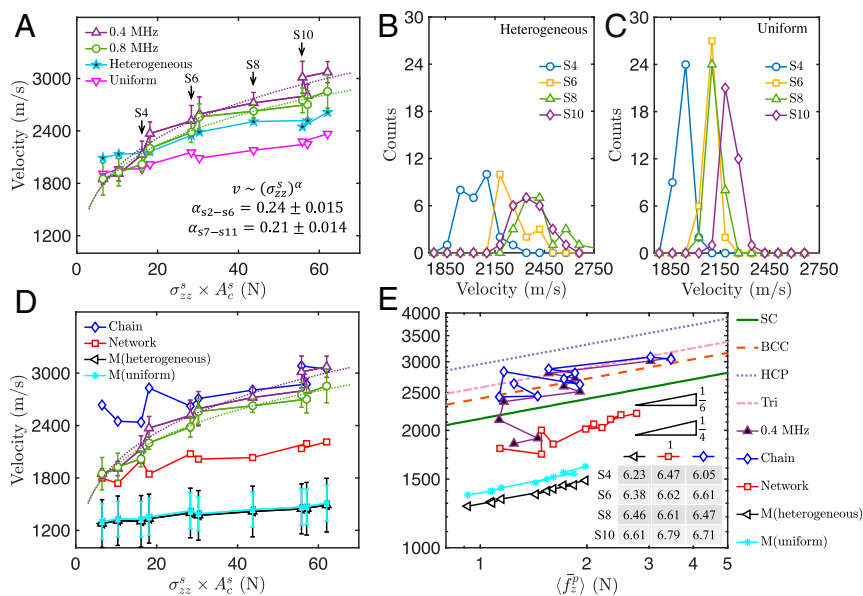
Fig. 1. Ultrasound velocities obtained by experimental measurements, simulations of network responses, and theoretical predictions. (A) Experimentally measured wave velocities (purple triangles for 0.40 MHz and green circles for 0.80 MHz) compared with simulations (blue stars and magenta inverted triangles). Error bars are the SD across the five measurements. Histograms of simulated velocities calculated for each particle contacting the bottom platen, as described in the text, for heterogeneous (B) and uniform (C) networks at load steps 4, 6, 8, and 10. In simulations, a single half-period of a sinusoidal with a fixed frequency of 0.4 MHz was used as the input signal at the top platen. (D) Experimentally measured wave velocities (same symbols as A) compared with averaging unit cell velocities with heterogeneous [M(heterogeneous)] and uniform [M(uniform)] forces as well as unit cells with actual velocities but only constituting the fastest theoretical chain (Chain) and percolating force network (Network). (E) Dependence of theoretically estimated wave velocity on the effective vertical contact force calculated in three distinct ways and compared with isotropically loaded granular crystals. Dependence of experimentally measured wave velocities of 0.4 MHz on the effective vertical contact force for the fastest chain is shown by a black triangle.
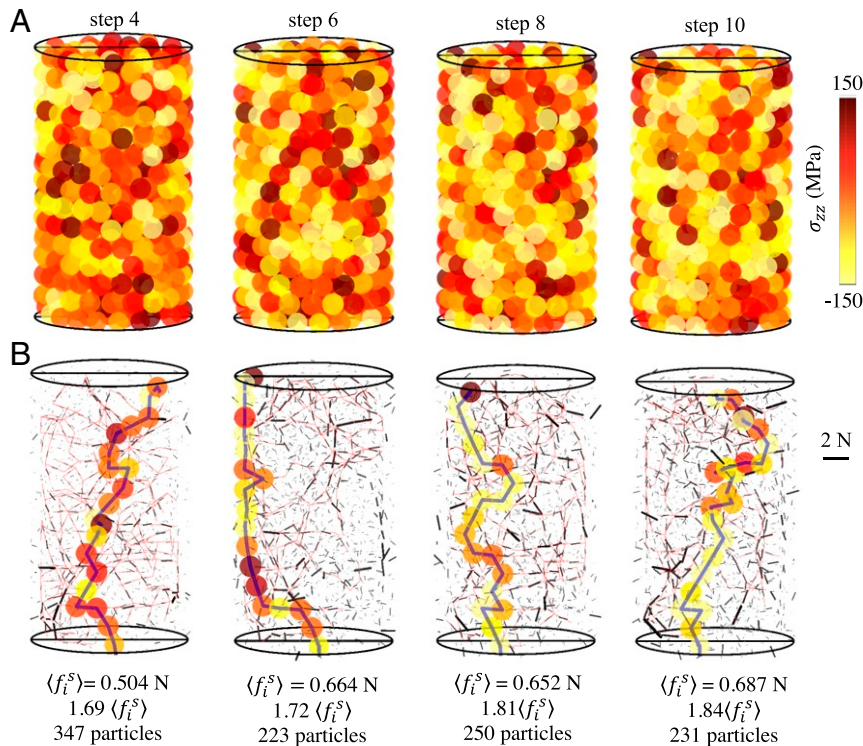
disorder and interparticle force network (called "heterogeneous") and for a separate spring network with measured structural disorder but uniform stiffness (called "uniform"). An input signal was put into the contact network by forcing all particles contacting the top platen to oscillate following a single half-period of a sinusoidal with a fixed frequency of 0.4 MHz. The sum of all contact forces on the bottom platen was taken to be the received signal. The same cross-correlation analyses used in experiments were used to measure the wave velocity through the material in simulations. The uniform network features a reduced total velocity compared with the heterogeneous network, reflecting the influence of the horizontally aligned forces (used in finding an average force and thus, average stiffness), which are typically lower than the vertically aligned forces. The network with heterogeneous forces exhibits a similar velocity scaling to experimental measurements, suggesting that both structural disorder and force heterogeneity are needed to precisely predict the acoustic velocity.

We further examined the contact forces between particles contacting the bottom platen in simulations. We calculated a wave velocity for each contacting particle by dividing the height of the sample by the time between the input signal peak and the first peak in the particle–platen force (25). Distributions of these velocities for load steps 4, 6, 8, and 10 for a 0.4-MHz input signal are provided in Fig. 1 B and C for the heterogeneous and uniform networks, respectively. A significantly broader spread is observed for the network containing heterogeneous forces (Fig. 1B), which cause local variations in the acoustic velocities and acoustic paths. This spread signifies the influence of

force heterogeneity on dispersion and loss of phase coherence, as described in the following sections.

To further understand the path of ultrasound waves propagating through the granular packing, we constructed a unit cell for each individual particle using the positions of its neighbors and the corresponding interparticle forces, extracted from X-ray measurements. We calculated the theoretical acoustic wave velocity in the vertical (z) direction through each unit cell. Based on this velocity, we estimated the sample's theoretical wave velocity by 1) averaging all unit cells' theoretical wave velocities using experimentally measured contact forces [labeled M(heterogeneous)] and uniform contact forces [labeled M(uniform)], 2) averaging only over unit cells corresponding to a percolating network of "strong" interparticle forces, and 3) identifying the fastest theoretical wave path or "chain" through the sample.

The percolating network of strong interparticle forces was identified as follows. First, a force threshold was specified, and all contacts with a force magnitude above that threshold were retained. Next, we searched for a continuous path through these contacts that connected the bottom platen to the top platen (ignoring lateral particle-boundary contacts). Finally, we incremented the force level by $+0.01\langle f_i^s \rangle$ with $\langle f_i^s \rangle$ being the average interparticle force magnitude across all contacts in the sample. The last force level for which a connected path could be found was identified as the force threshold (provided in Fig. 2B for load steps 4, 6, 8, and 10) for percolation, and the corresponding path was identified as the percolating network of strong interparticle forces. The velocity through the percolating network was

$\langle f_i^s \rangle = 0.504$ N
$1.69 \langle f_i^s \rangle$
347 particles

$\langle f_i^s \rangle = 0.664$ N
$1.72 \langle f_i^s \rangle$
223 particles

$\langle f_i^s \rangle = 0.652$ N
$1.81 \langle f_i^s \rangle$
250 particles

$\langle f_i^s \rangle = 0.687$ N
$1.84 \langle f_i^s \rangle$
231 particles

Fig. 2. Particle stresses, force networks, and the fastest ultrasound wave paths. (A) The vertical component of individual particle stress, σ_{zz}^p, at load steps 4, 6, 8, and 10. Stress values are indicated by the color. The positions of all 621 grains were determined from XRCT measurements at each load step. Particle stresses were calculated based on per-particle strain tensor measured from 3DXRD and the anisotropic elastic constants for the used sapphire material. More details regarding XRCT and 3DXRD measurements can be found in *SI Appendix*, section 1. (B) Contact forces at load steps 4, 6, 8, and 10 for all contacts (in black), percolating networks of strong interparticle forces (in red), and particle chains with the shortest time of fight (particles colored with σ_{zz}^p). Contact forces (in black) are rendered with the same linear scaling factors for length, width, and opacity for all load steps. Elements of the percolating network of strong interparticle forces and the fastest chains are lines connecting centers of particles in contact. The average contact forces throughout the sample, $\langle f_i^s \rangle$, are 0.504, 0.664, 0.652, and 0.687 N, respectively; force threshold values for percolating networks are $1.69\langle f_i^s \rangle$, $1.72\langle f_i^s \rangle$, $1.81\langle f_i^s \rangle$, and $1.84\langle f_i^s \rangle$, respectively; and numbers of particles connected in force percolation networks are 347, 233, 250, and 231 at load steps 4, 6, 8 and 10, respectively.

computed by averaging the velocity in the z direction across all unit cells whose central particles belong to this network (the numbers of particles in networks for load steps 4, 6, 8, and 10 are provided in Fig. 2B).

The fastest theoretical chain, called chain in Fig. 1, was obtained by comparing all possible acoustic paths through the sample from the top to bottom platen. One particle contacting the top platen was labeled as the first particle of this acoustic path. Any particles contacting this first particle with a z position lower than the first particle's z position were treated as a viable path for wave transmission. This process was repeated until a path from the top platen to the bottom platen was constructed. All such paths were evaluated, and the time of flight for each path was computed by $\frac{1}{2} \sum_{i=1}^{N^{\text{chain}}} t_z^i$, where $t_z^i = h_z^i / v_z^p$, with h_z^i being the vertical distance between centroids of the two particles in the chain above and below particle p, and v_z^p being the longitudinal wave velocity of the unit cell for the particle, p. The factor of $\frac{1}{2}$ was used because the wave travel distance of h_z^i was counted twice in the calculation. Among all paths, the chain demonstrating the shortest time of flight was defined as the fastest chain. The sample height at each load step was divided by the shortest time of flight to determine the theoretical velocity on this fastest wave path. Force percolation networks and the fastest chain for load steps 4, 6, 8, and 10 are provided in Fig. 2B.

Velocity predictions by all three methods (averaging over unit cells, on percolating strong force networks, through fastest chains) are shown in Fig. 1D, along with experimentally measured velocities. Velocities obtained for the fastest chain and the force percolation network, respectively, served as approximate upper and lower bounds for the experimentally measured velocities. The fastest chain prediction closely matched measured wave velocities, particularly at high loads. This finding indicates that the actual force magnitudes on the fastest chain are needed to explain the wave speed of the coherent pulse. In contrast, the predicted velocities averaged over all unit cells for both M(uniform) and M(heterogeneous) fall far below the measured wave velocities. The case of M(uniform) resulted in similar velocities to those of M(heterogeneous) and demonstrated smaller deviations. This finding indicates that averaging over all particles' structural disorder and force heterogeneity when making velocity predictions is not appropriate, as such averaging significantly reduces expected wave speeds.

The three velocity predictions employ contact networks with different levels of average contact force and different levels of structural disorder. As illustrated in Fig. 2B, the percolating force network and fastest paths tend to develop along contacts with higher than average contact forces and particles with higher than average vertical compressive stress magnitudes. To further emphasize the role of contact forces in furnishing wave velocities, we evaluated the scaling of both the predicted and measured velocities with respect to the effective vertical contact force, $\bar{f}_z^p$. The effective vertical contact force was calculated as the sum of the vertical forces on each particle, p, along the wave path (entire sample, percolating force network, or fastest chain). $\bar{f}_z^p$ is calculated by

$$\bar{f}_z^p = \left(\left(\sum_{c=1}^{N_c^p} \|\boldsymbol{f}^c\| \boldsymbol{a}_i^c \boldsymbol{a}_j^c \right) \boldsymbol{e}_z \right) \cdot \boldsymbol{e}_z, \quad \text{[1]}$$

where subscripts indicate tensor indices, $\boldsymbol{e}_z$ is the unit vector $(0, 0, 1)^T$, $\boldsymbol{a}^c$ is a unit vector parallel to the contact force, pointing to particle p, and $\boldsymbol{f}^c$ is the force vector acting on particle p. Note that the term in the inner parentheses is the force-weighted fabric tensor. As is shown in Fig. 1E, the predicted and measured velocities with different methods generally follow power-law relationships with $\langle \bar{f}_z^p \rangle$, showing different exponents.

An exponent of about 0.18 was found for experimentally measured wave velocities (at 0.4 MHz) plotted against vertical forces on the fastest chain across load steps 4 to 11. For comparison, the experimentally measured coherent wave velocities scaled with the average vertical forces on the percolating force network with a power-law exponent of 0.39 and with the average forces on all contacts with a power-law exponent of 0.53 (neither is shown in Fig. 1). This demonstrates that the fastest chain is the only path of those considered that follows the expected Hertzian velocity scaling of 1/6.

We note that the apparent Hertzian scaling of wave velocity with the effective vertical contact force on the fastest chain, $\langle \bar{f}_z^p \rangle$, suggests an alternative, unexplored explanation for the transition of power-law exponent from 1/4 to 1/6. Specifically, the coherent wave may follow Hertzian predictions of a 1/6 power-law scaling microscopically (i.e., with $\langle \bar{f}_z^p \rangle$) across a broad range of macroscopic loads. However, the value of $\langle \bar{f}_z^p \rangle$ may scale nonlinearly with macroscopic sample pressure, σ_{zz}, because interparticle forces tend to become more homogeneous under increasing macroscopic pressure (9, 10, 48, 49). The tendency of interparticle forces to become more homogeneous with load suggests that larger increments in macroscopic pressure may be needed at higher loads to induce similar increments in $\langle \bar{f}_z^p \rangle$ on the fastest chain. This implies that the scaling exponent of wave velocity with $\langle \bar{f}_z^p \rangle$ should decrease with sample compression, which is reflected in the widely observed 1/4 to 1/6 scaling transition (28). This possibility will be addressed in future research and is not studied further here. A number of particles fractured during the experiment (detailed in *SI Appendix*, section 1A). The resulting fragments potentially introduce different contact laws and thus, different force-dependent velocity scaling. Other factors related to the contact law between particles, including rough contact (50), plastic deformation of particle contacts (8), and particle shape (27), can also contribute to the transition of the exponent value and were not investigated here.

The wave velocities predicted with the three methods described above were also compared in Fig. 1E with theoretical acoustic velocities of granular crystals to further evaluate the role of structural disorder. The granular crystals included simple cubic (SC; equivalent to monatomic chain), body-centered cubic (BCC), hexagonal close packed (HCP), and a 2D triangular lattice (Tri). Experimentally measured wave velocities for most load steps lie between those for SC and HCP structures and closely follow BCC predictions across load steps 4 to 11. This suggests that a BCC structure can be used to predict the scaling of ultrasound wave velocity with force at sufficient large force levels. However, the chain prediction more closely tracks the particular variations in the scaling of measured velocities with force, indicating that the particular details of local structure and force magnitudes on this chain can significantly improve predictions.

Wave Dispersion. To study wave dispersion, we computed spectrograms of received signals through the granular sample, received signals through pistons in contact, and received signals through simulated lattice networks. Corresponding spectrograms are shown in Fig. 3 *A–D* for the input signal of 0.8 MHz at load step 8. For the simulations (Fig. 3 *C* and *D*), experimental input signals (i.e., the Gaussian bursts shown in Fig. 7A) were scaled to limit the maximum particle displacement to <1 μm and injected into the heterogeneous and uniform networks. In both the experimental and numerical settings, wave reflection on the boundaries (e.g., platen–particle boundary at the top of the sample) cannot be avoided due to the sample size. Therefore, the spectrogram analysis is only performed for the first 5 μs (including three to five wave cycles) after the arrival of the
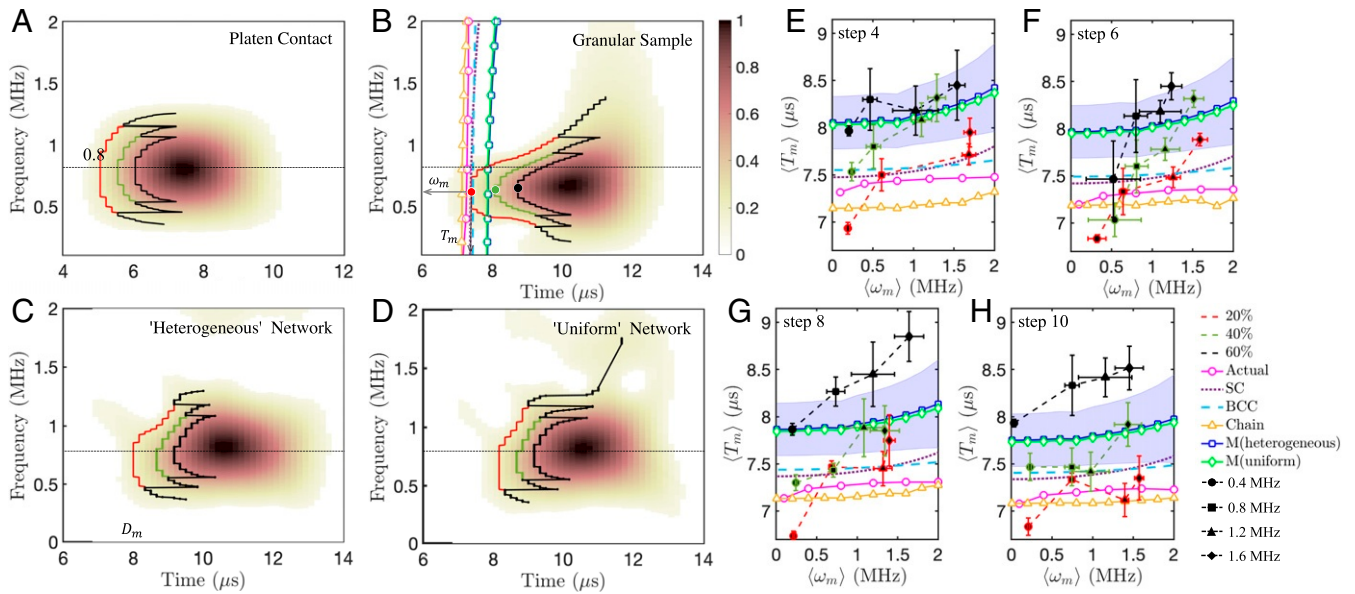
Fig. 3. Comparison of wave dispersion obtained from experiments, simulations, and theoretical predictions. (*A*) Spectrogram of the 800-kHz received signal averaged over 10 measurements with top and bottom platens in contact. (*B*) Spectrogram of the 800-kHz received signal averaged over five measurements through sample at load step 8. Spectrograms from simulations based on heterogeneous (*C*) and uniform networks (*D*). (*E–H*) Dispersion relations based on experimental measurements, theoretical predictions by averaging unit cells for the entire packing [M(heterogeneous)] and the fastest chain (chain), and simulations with heterogeneous network for load steps 4 (*E*), 6 (*F*), 8 (*G*), and 10 (*H*). Dispersion relations for SC and BCC granular crystals are shown for reference.

coherent wave to minimize the effects of wave reflection, as in ref. 16. Contour lines at 20, 40, and 60% of the maximum signal amplitude in the first 5 μs of wave analysis are also shown in Fig. 3 *A–D*.

Theoretical dispersion predictions from averaging unit cell dispersion relations across the entire packing (with actual interparticle forces) and across only particles in the fastest chain are shown in Fig. 3 *E–H* as blue lines with square makers (the shaded region represents ±1 SD of arrival times) and brown lines with triangle markers, respectively. Results based on unit cells with uniform force are shown in green lines with diamond markers, the error bars of which (not shown) are slightly smaller than those for the unit cells with the actual interparticle forces. The dispersion relations based on network simulations are presented in pink lines with circle markers. Dispersion relations based on isotropically loaded SC and BCC granular crystals (having comparable coordination number with the studied sample) are provided for reference. For comparison, the numerical and analytical results were shifted to a common time axis with the experimental observations by adding the time of flight for the case of piston contact.

Compared with the input signal (similar to Fig. 3*A*), the spectrograms of received signals for experiments (Fig. 3*B*) and simulations (Fig. 3 *C* and *D*) demonstrated significant distortion indicative of dispersion, with delayed higher-frequency components. The earliest time, T_m, and corresponding characteristic frequency, ω_m, of spectrogram contours at 20, 40, and 60% of the maximum spectrogram amplitude are highlighted by dots in Fig. 3*B*, indicating frequency-dependent wave arrival time. These points are plotted for all input frequencies at load steps 4, 6, 8, and 10 in Fig. 3 *E–H*, with error bars representing SDs of ω_m and T_m across the five measured output signals. Wave dispersion can clearly be seen in these figures, with higher-frequency content arriving at the receiver after lower-frequency content.

The measured dispersion varies significantly, not closely following any particular theoretical prediction. However, the trend of the curves, particularly for the 60% contours, more closely fol-

lows that from the average of unit cells in the entire packing with actual or uniform forces (green or blue curves) than, for instance, that of the fastest chain (brown curve). Specifically, the experimentally measured dispersion is stronger (i.e., arrival time is more delayed with frequency) than that predicted from the fastest chain. This suggests that the details of the entire packing, rather than the subset supporting the fastest wave, are needed to predict dispersion.

To highlight the importance of force heterogeneity on dispersion, we made further dispersion predictions by averaging the power spectrum of all particles in the spring networks with heterogeneous and uniform forces after inputting an initial condition. The dispersion for the heterogeneous network is shown in Fig. 4*A* and demonstrates a broader spread than that for the uniform network shown in Fig. 4*B*, emphasizing enhanced loss of phase coherence for the excited modes due to force heterogeneity.

Wave Attenuation. Attenuation of input signals was evaluated by the transmission ratio as a function of input frequency and load step, as shown in Fig. 5*A*. We define the transmission ratio as the ratio of maximum spectrogram amplitude of the received signal (in arbitrary units) through the granular packing to that of the
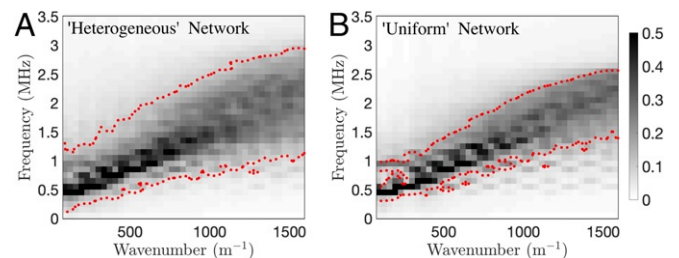
Fig. 4. Dispersion relations at load step 8 based on (*A*) inferred contact force and (*B*) force-uniform contact fabric. Red dotted lines indicate contour at 10% of the maximum amplitude.
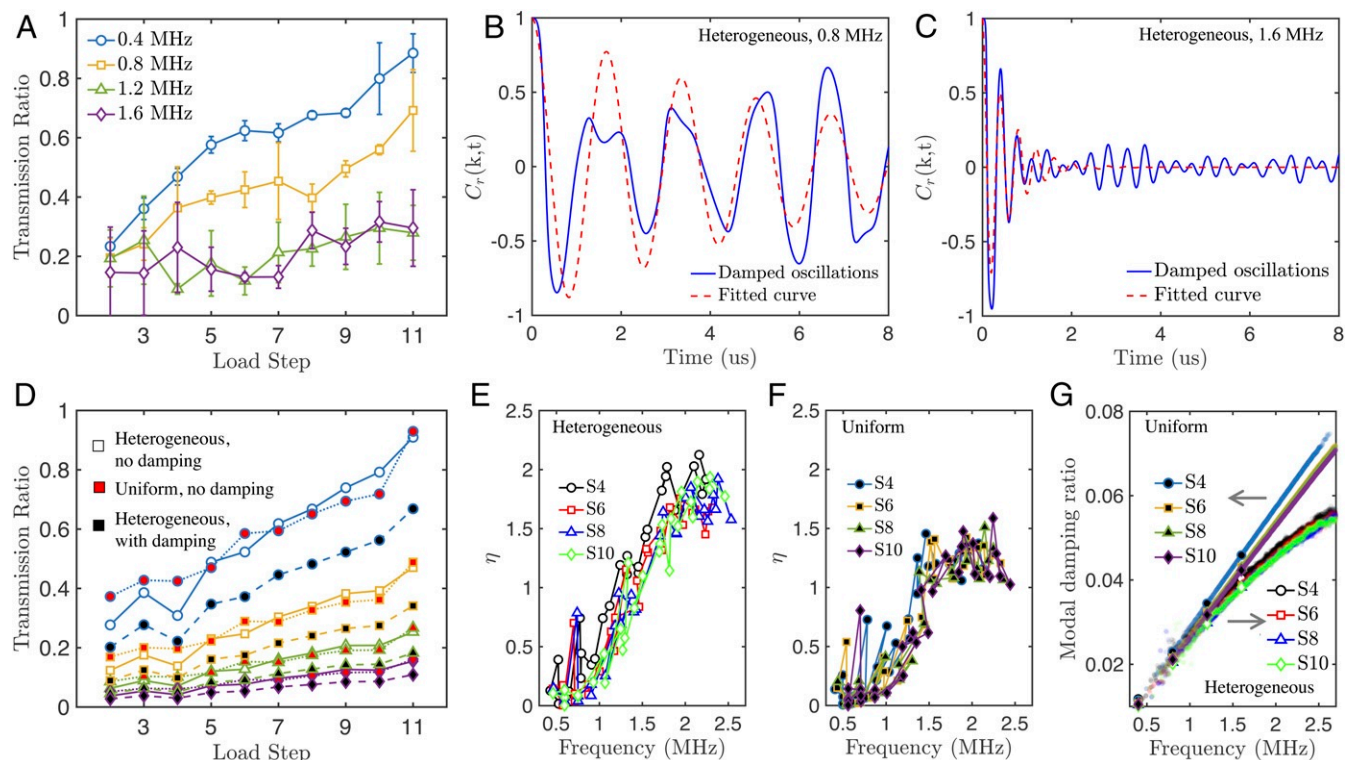
Fig. 5. Wave attenuation due to scattering and viscous contact damping. (*A*) Transmission ratio for experiments with four different input signals across load steps. Error bars represent SDs across five measurements. Damped oscillations with different initial conditions (*SI Appendix*, section 4A) for $2\kappa\langle r_i\rangle = 0.2\pi$ (*B*) and $2\kappa\langle r_i\rangle = 0.7\pi$ (*C*), corresponding to 0.8 and 1.6 MHz, respectively, at load step 8. (*D*) Comparison of transmission ratios for the contact network with inferred forces ($\mathcal{C} = 0$), the contact network with uniform forces ($\mathcal{C} = 0$), and the contact network with inferred forces ($\mathcal{C} \neq 0$). The colors and markers are the same as in *A* for the different input frequencies. (*E* and *F*) Attenuation coefficients due to wave scattering for case of inferred forces (*E*) and uniform forces (*F*). (*G*) Modal damping ratios for both cases of inferred forces (markers with white faces) and uniform forces (markers with black faces).

received signal through the pistons in contact with one another (this latter amplitude is nearly frequency- and compression-level independent). The transmission ratio is below 0.3 at nearly all load levels for input frequencies 1.2 and 1.6 MHz. The transmission ratio rises above 0.5 and close to 1.0 at the highest load levels for input frequencies of 0.4 and 0.8 MHz. We suspect the observed attenuation arises mainly from two mechanisms: Rayleigh scattering (20, 21) and viscoelastic damping at particle contacts (44, 47, 51).

To evaluate attenuation due to Rayleigh wave scattering, we calculated the scattering attenuation coefficient (*SI Appendix*, section 4A), η, by fitting autocorrelation functions of the longitudinal velocity with $C_l = e^{-\eta(\kappa)t}\cos(\omega_d\kappa t)$ for different initial conditions controlled by wave number κ as in refs. 20 and 21. For viscoelastic damping at particle contacts, we employed a proportional (also called Rayleigh but unrelated to Rayleigh scattering) damping model (52) and defined a damping matrix $\mathcal{C}$ linearly proportional to the mass and stiffness matrices $\mathcal{C} = c_m\mathcal{M} + c_h\mathcal{H}$ where c_m and c_h are the mass and stiffness proportional damping coefficients ($c_m, c_h \geqslant 0$), accounting for the damping arising from background motion resistance (e.g., drag) and particle contacts, respectively (47). The background damping was ignored in this study. We adopted a viscoelastic Hertzian contact model (45, 46) for dissipation at each individual contact along both normal and tangential directions, yielding a damping matrix $\mathcal{C}$ proportional to $\mathcal{H}$. The network response with damping was then obtained by integrating Eq. **6** using the ODE45 solver in Matlab. Modal damping ratios, ζ, were computed by $\zeta = \frac{1}{2}[\boldsymbol{\Phi}^T\mathcal{C}\boldsymbol{\Phi}]\boldsymbol{\Omega}^{-1}$ where $\boldsymbol{\Phi}$ is the undamped modal matrix, $\boldsymbol{\Omega}$ is a diagonal matrix containing undamped natural frequencies of the system, and ζ is a diagonal matrix containing a damping ratio for each mode.

Modal damping factors indicate whether the system is undamped ($\zeta = 0$), damped ($0 < \zeta < 1$), critically damped ($\zeta = 1$), or overdamped ($\zeta > 1$).

To study the relative impact of interparticle dissipation and Rayleigh scattering on wave attenuation, we compared the measured wave attenuation with three types of simulations: 1) network simulations with inferred forces and $\mathcal{C} = 0$, 2) network simulations with uniform forces and $\mathcal{C} = 0$, and 3) network simulations with inferred forces and $\mathcal{C} \neq 0$. Sinusoidal pulses of a single half-period with frequencies of 0.4, 0.8, 1.2, and 1.6 MHz were injected into the top platen, and the sum of contact forces on the top platen and the bottom platen over all contacting particles was recorded. The transmission ratio was calculated as the ratio of the magnitude of the first peak in the sum of contact forces received at the bottom platen to the magnitude of the first peak of input signal at the top platen. As compared in Fig. 5*D*, we observed 1) increasing transmission ratios, thus decreasing attenuation, with increasing compression; 2) more attenuation with increasing frequency; 3) comparable transmission ratios for contact networks with heterogeneous and uniform forces; 4) a slight increase in wave attenuation due to interparticle dissipation; and 5) Rayleigh scattering as the main attenuation mechanism, capable of explaining much of the experimentally observed attenuation.

To further demonstrate these points, we present attenuation coefficients due to scattering in Fig. 5 *E* and *F* and the modal damping ratio due to interparticle dissipation in Fig. 5*G*. The attenuation coefficient due to scattering on a uniform network (Fig. 5*F*) was slightly lower than that of the heterogeneous one (Fig. 5*E*) for high frequencies, suggesting that disorder due to force heterogeneity only slightly enhances attenuation due to

wave scattering. Examples of velocity correlation calculations for the scattering-only case (no contact damping) with different initial conditions are shown in Fig. 5 *B* and *C* to illustrate the dominant role of wave scattering on wave attenuation. On the other hand, for all frequencies between 0 and 3 MHz, ζ was found to be smaller than 0.07 with a restitution coefficient of 0.9 [within ranges tabulated for sapphire (53)], suggesting the secondary role of interparticle damping in attenuation, as first illustrated in Fig. 5*G*.

Conclusions

In this study, ultrasound responses of externally stressed disordered granular materials were experimentally and numerically investigated. Gaussian burst ultrasound waves with different center frequencies were sent through a disordered 3D granular material compressed to different levels of sample stress. In situ XRCT and 3DXRD enabled the measurement of contact fabric, crystal orientation, average intraparticle stress tensors, and interparticle forces at the corresponding levels of sample stress. The packing configuration and inferred interparticle forces were used to construct a linear spring network. The ultrasound response of this network was simulated to quantitatively determine the relative importance of packing structure disorder and interparticle force heterogeneity in controlling wave velocity, acoustic paths, dispersion, and attenuation. The findings of this study are summarized as follows.

1) The experimentally measured velocity of the coherent wave was quantitatively predicted by the theoretical fastest velocity on any chain through the packing and scaled with interparticle forces measured on this chain according to Hertzian contact theory. We conclude that both the packing disorder and interparticle force heterogeneity are responsible for ultrasound wave velocities and velocity scaling in disordered granular media.

2) Experimentally measured velocities were found to be dependent on frequency, indicating significant dispersion. No dispersion predictions closely matched those that were experimentally measured. Simulations with uniform and heterogeneous forces suggested that packing disorder significantly increases dispersion, with force heterogeneity playing a secondary role primarily discernible in dispersion relation plots. We conclude that packing disorder is primarily responsible for dispersion, with force heterogeneity playing a secondary role.

3) Additionally, the measured force heterogeneity and corresponding simulation results suggest that wave attenuation was primarily due to wave scattering. Force heterogeneity enhanced loss of phase coherence but played a negligible role in overall wave attenuation. Therefore, we conclude that packing disorder is primarily responsible for attenuation of longitudinal ultrasound waves.

The findings of this research provide insight into the microscopic features associated with particular wave behaviors and may support the development of materials for wave manipulation and methods for nondestructive testing.

Materials and Methods

Experimental Setup. The granular material we studied was a sample of 621 single-crystal sapphire spheres (Bird Precision) with radii ranging from 94 to 103 μm and uniform roughness below 15 nm (for rms roughness of the particle surface). The granular material was prepared by pouring particles into an aluminum cylinder of 1.5-mm inner diameter, 3.00-mm outer diameter, and 8-mm height. The sample developed locally crystallized regions but was largely disordered. The sample was then placed in a custom-built uniaxial load frame described next and shown in Fig. 6*A*. The load frame features a linear actuator with encoder (Haydon Kerk Size 34 Stepper Motor), a broadband piezoelectric transducer and receiver (Olympus V133-RM), each in an aluminum encasement, stainless steel compression platens, and a load cell (Futek LCM200), all mounted to an aluminum plate and a polycarbonate tube. To drive and monitor the load frame components, we employed a National Instruments (NI) system, which contained a computer (PXIe-1082

Express Chassis), a motion controller (PXI-7342 and UMI-7764), an arbitrary waveform generator (PXIe-5423), and an oscilloscope (60 MHz; PXIe-5105). The system is shown in its operational configuration outside the X-ray hutch in Fig. 6*B*. The load frame was mounted on the translation and rotation stage present at the Advanced Photon Source (APS) beamline 1-ID-E (Fig. 6*C*) throughout the experiment, and XRCT and 3DXRD measurements were performed between increments of sample strain. Fig. 6*D* illustrates the experimental geometry schematically.

Mechanical Loading. The granular sample was loaded mechanically in small strain increments, ranging from 0.005 to 0.01, by microstepping the linear actuator, which drove the stainless steel platen located above the granular material downward in the $-z$ direction. The loading rate was limited to approximately 1 μm/s to ensure that the loading remained quasistatic (strain rate of 10^{-3} to 10^{-4}). After each increment of mechanical loading, XRCT and 3DXRD measurements were performed, followed by an ultrasound frequency sweep.

Ultrasound Transmission. After each 3DXRD measurement, an ultrasound signal was transmitted through the sample using the piezoelectric transducer above the sample. The signal was received using the piezoelectric receiver below the sample. Four types of signals were transmitted, each of which was transmitted and received five times. Each signal was generated by sending a time-varying voltage to the piezoelectric transducer: a sinusoid convolved with a Gaussian, yielding "Gaussian bursts" (16) with center frequencies of 0.40, 0.80, 1.20, and 1.60 MHz. The center frequencies were selected to fall below the cutoff frequencies of a 1D chain of 200-μm diameter sapphire spheres under axial compression of 0.50 N, which were calculated to be 3.27 MHz (*SI Appendix*, section 5). Features of input signals (in the time domain and frequency domain) are provided in Fig. 7 *A* and *B*. Note that all frequencies used in this study are angular frequencies unless otherwise specified.

Wave velocities for the coherent portion of transmitted waves were calculated by combining cross-correlation analysis of the average received signals and the input signal and cross-correlation analysis of the signals received themselves (*SI Appendix*, section 1C). The resulting cross-correlation coefficients at center frequencies of 0.4 and 0.8 MHz typically featured a sharp rise at the arrival of the coherent signal. However, this sharp rise could not be captured in some signals with center frequencies of 1.2 and 1.6 MHz that demonstrated significant attenuation. At these frequencies, we therefore inspected the received signals, and we selected a peak in the
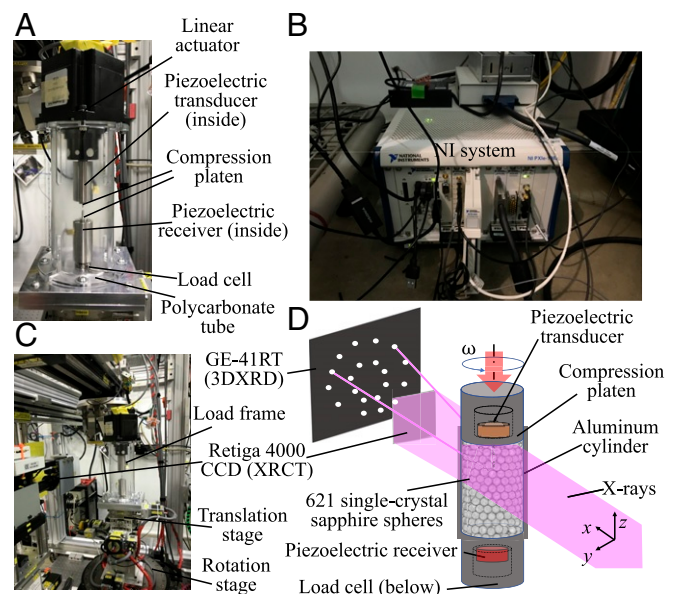
Fig. 6. Schematic of experimental setup. (*A*) Picture of the load frame mounted at the APS showing major components. (*B*) NI system in operational configuration outside X-ray hutch. (*C*) Load frame mounted at the APS. (*D*) Experimental geometry, showing the sample and coordinate frame. ω corresponds to the rotation of the entire load frame during X-ray measurements.
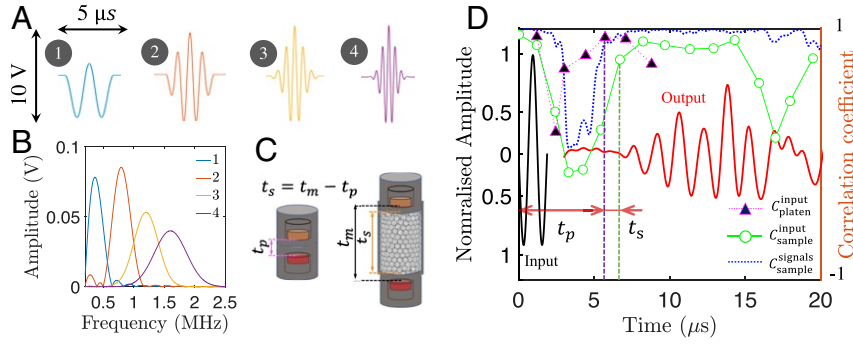
Fig. 7. Features of input signals and calculation of wave velocities. Gaussian burst signals with center frequencies of 0.40, 0.80, 1.20, and 1.60 MHz in the time (*A*) and frequency (*B*) domains. (*C*) Time of flight through sample and pistons, t_m (*Left*), and pistons in contact, t_p (*Right*). (*D*) Transmitted ultrasound signals for input Gaussian bursts centered at 0.8 MHz at step 7. Input signal (black) and average received signal through sample and platens (red) correspond to the left *y* axis. Cross-correlation between the average of received signals and input (green circles), cross-correlation between received signals through sample (blue dashed line), and cross-correlation between the signal through platens in contact and input (magenta triangles) use the right *y* axis.

cross-correlation that corresponded to a cross-correlation below 0.75 but was consistent with arrival times at previous load levels. To compute the wave speed through the granular sample, we subtracted the arrival time of the coherent wave obtained from two pistons in contact, t_p, from the arrival time through the sample, t_m, and divided the sample height (identified by the separation distance of the loading platens in XRCT images) by the result, $t_s = t_m - t_p$.

Inference of Interparticle Forces. By combining XRCT and 3DXRD datasets, all interparticle and particle-boundary force vectors were calculated using a modified version of the minimization procedure described in refs. 9, 10, 54, and 55. The minimization procedure involved an effort to satisfy equilibrium (Eqs. **2** and **3**) and stress–force relations (Eq. **4**) for each particle:

$$\sum_{i=1}^{N_c^p} \boldsymbol{f}^i = 0, \qquad [2]$$

$$\sum_{i=1}^{N_c^p} \boldsymbol{x}^i \times \boldsymbol{f}^i = 0, \qquad [3]$$

$$\sum_{i=1}^{N_c^p} \Lambda^p \boldsymbol{x}^i \otimes \boldsymbol{f}^i = \Lambda^p V^p \boldsymbol{\sigma}^p, \qquad [4]$$

where N_c^p is the total number of contacts for particle *p*, $\boldsymbol{f}^i$ is the force vector at contact *i*, and $\boldsymbol{x}^i$ is the position of the contact *i*. A parameter $\Lambda^p = \sigma_h^p/\langle\sigma_h^s\rangle$ was calculated with $\sigma_h^p = (\sigma_{xx}^p + \sigma_{yy}^p + \sigma_{zz}^p)/3$ and $\langle\sigma_h^s\rangle = \langle(\sigma_{xx}^s + \sigma_{yy}^s + \sigma_{zz}^s)/3\rangle$ being the per-particle and sample-averaged (average indicated with $\langle\cdot\rangle$) hydrostatic stress, respectively. This parameter weakened the contribution of particles with small measured stress values (within the noise level of measurements) in the weighted objective function that was minimized to find contacts forces:

$$\|\boldsymbol{K}_{st}\boldsymbol{f} - \boldsymbol{b}_{st}\|_2 + \lambda\|\boldsymbol{K}_{eq}\boldsymbol{f}\|_2. \qquad [5]$$

In this objective function, $\|\ldots\|_2$ is the 2-norm, $\boldsymbol{K}_{st}$ (corresponding to Eq. **4**) and $\boldsymbol{K}_{eq}$ (corresponding to Eqs. **2** and **3**) are $6N_p^s \times 3N_c^s$ matrices containing positions of all grains and contacts in the packing, $\boldsymbol{b}_{st}$ is a $6N_p^s$ vector containing all per-particle stresses, $\boldsymbol{f}$ is a N_c^s vector containing all contact forces of the packing, and λ is a trade-off parameter. This information is also available in refs. 9, 10, 56, and 57, but it is summarized here and detailed in *SI Appendix*, section 2. We denote the overall number of contacts in the system $N_c^s = \sum N_c^p$. In the minimization procedure, a Coulomb friction constraint on each interparticle contact force vector was also enforced: $f_t^i \leq \mu f_n^i$, where f_t^i is the tangential force component and f_n^i is the normal force component at contact *i*. The friction coefficient was assumed to be 0.2 for both sapphire–sapphire and sapphire–boundary contacts (58). Future work will quantify this friction coefficient and its variability with separate small-scale sliding experiments in the same load and ambient humidity range present in the experiments, similar to those performed by others (59). Renderings of contact forces at select load steps are provided in Fig. 2*B*. These renderings employ linear scaling of force vector lengths, widths, and opacities with force vector magnitude.

Dynamical Responses of Contact Network. With the experimentally measured contact network and interparticle forces described above, we constructed a spring network to further study the system's dynamical response at each level of applied sample stress in the experiment (20, 21). We assumed that the contact fabric remained unchanged by wave propagation. We further assumed that, during ultrasound wave propagation, particles oscillated with respect to their equilibrium positions (identified experimentally). Finally, we calculated a linear contact stiffness at each interparticle contact by linearizing a Hertzian contact law at the measured interparticle force.

The governing equations of wave propagation in the granular sample are given by

$$\mathcal{M}\ddot{\boldsymbol{u}}(t) + \mathcal{C}\dot{\boldsymbol{u}}(t) + \mathcal{H}\boldsymbol{u}(t) = 0, \qquad [6]$$

where $\mathcal{M}$, $\mathcal{C}$, and $\mathcal{H}$ are the mass, damping, and Hessian matrices, each with dimensions $6N_p^s \times 6N_p^s$; $\boldsymbol{u}$ is $6N_p^s \times 1$ vector containing the displacement and rotational configuration of all particles relative to their reference positions; $\boldsymbol{u}(t) = [\ldots, x_p(t), y_p(t), z_p(t), \theta_p(t), \beta_p(t), \gamma_p(t), \ldots]$; and *t* is time. Matrices of $\mathcal{M}$, $\mathcal{C}$, and $\mathcal{H}$ are described in detail in *SI Appendix*, section 3 and were notably constructed using the experimentally measured packing structure and in some calculations, the experimentally measured interparticle forces. Eq. **6** was numerically integrated using the ordinary differential equation solver ODE45 in Matlab, for given initial conditions.

We focused numerical simulations on studying longitudinal wave propagation along the vertical (*z*) direction of the sample to mirror input and output signals controllable and measurable in experiments. To investigate the relative influence of packing structure and interparticle force heterogeneity on observed wave behaviors, we simulated wave propagation in two ways. The first way used both the experimentally measured contact networks and interparticle forces in the construction of mass, damping, and Hessian matrices. The second way used the experimentally measured contact network but assumed a uniform contact stiffness, derived from the average interparticle force in the packing, at all interparticle contacts. Although the latter system would be out of equilibrium if its interparticle contact forces were derived from the corresponding interparticle stiffness values, it provided a convenient method of decoupling the influence of force heterogeneity from that of structural disorder. Further theoretical calculations with granular crystals then provided a comparison of these results with scenarios without structural disorder.

PHYSICS

1. I. L. Vér, "Interaction of sound waves with solid structures (Chap. 11)" in *Noise and Vibration Control Engineering: Principles and Applications*, I. L. Vér, L. L. Beranek, Eds. (John Wiley & Sons, Inc., Hoboken, NJ 2005), pp. 389–515.
2. P. A. Johnson, X. Jia, Nonlinear dynamics, granular media and dynamic earthquake triggering. *Nature* **437**, 871–874 (2005).
3. E. Riera *et al.*, Mass transfer enhancement in supercritical fluids extraction by means of power ultrasound. *Ultrason. Sonochem.* **11**, 241–244 (2004).
4. G. Michlmayr, D. Cohen, D. Or, Sources and characteristics of acoustic emissions from mechanically stressed geologic granular media—a review. *Earth Sci. Rev.* **112**, 97–114 (2012).
5. G. Gantzounis, M. Serra-Garcia, K. Homma, J. Mendoza, C. Daraio, Granular metamaterials for vibration mitigation. *J. Appl. Phys.* **114**, 093514 (2013).
6. H. M. Jaeger, S. R. Nagel, R. P. Behringer, Granular solids, liquids, and gases. *Rev. Mod. Phys.* **68**, 1259–1273 (1996).
7. T. S. Majmudar, R. P. Behringer, Contact force measurements and stress-induced anisotropy in granular materials. *Nature* **435**, 1079–1082 (2005).
8. V. Nesterenko, *Dynamics of Heterogeneous Materials* (Springer Science & Business Media, 2013).
9. R. Hurley, S. Hall, J. Andrade, J. Wright, Quantifying interparticle forces and heterogeneity in 3d granular materials. *Phys. Rev. Lett.* **117**, 098005 (2016).
10. C. Zhai, E. Herbold, S. Hall, R. Hurley, Particle rotations and energy dissipation during mechanical compression of granular materials. *J. Mech. Phys. Solid.* **129**, 19–38 (2019).
11. S. Luding, Granular media: Information propagation. *Nature* **435**, 159–160 (2005).
12. M. Hiraiwa, S. Wallen, N. Boechler, Acoustic wave propagation in disordered microscale granular media under compression. *Granul. Matter* **19**, 62 (2017).
13. E. Herbold, J. Kim, V. Nesterenko, S. Wang, C. Daraio, Pulse propagation in a linear and nonlinear diatomic periodic chain: Effects of acoustic frequency band-gap. *Acta Mech.* **205**, 85–103 (2009).
14. B. P. Lawney, S. Luding, Frequency filtering in disordered granular chains. *Acta Mech.* **225**, 2385–2407 (2014).
15. B. Gilles, C. Coste, Low-frequency behavior of beads constrained on a lattice. *Phys. Rev. Lett.* **90**, 174302 (2003).
16. C. Coste, B. Gilles, Sound propagation in a constrained lattice of beads: High-frequency behavior and dispersion relation. *Phys. Rev.* **77**, 021302 (2008).
17. A. Merkel, S. Luding, Enhanced micropolar model for wave propagation in ordered granular materials. *Int. J. Solid Struct.* **106**, 91–105 (2017).
18. H. Cheng, S. Luding, K. Saitoh, V. Magnanimo, Elastic wave propagation in dry granular media: Effects of probing characteristics and stress history. *Int. J. Solid Struct.* (2019).
19. E. Wang *et al.*, High-amplitude elastic solitary wave propagation in 1-d granular chains with preconditioned beads: Experiments and theoretical analysis. *J. Mech. Phys. Solid.* **72**, 161–173 (2014).
20. S. Gelin, H. Tanaka, A. Lemaître, Anomalous phonon scattering and elastic correlations in amorphous solids. *Nat. Mater.* **15**, 1177–1181 (2016).
21. K. Saitoh, R. K. Shrivastava, S. Luding, Rotational sound in disordered granular materials. *Phys. Rev.* **99**, 012906 (2019).
22. P. Poorsolhjouy, A. Misra, Granular micromechanics based continuum model for grain rotations and grain rotation waves. *J. Mech. Phys. Solid.* **129**, 244–260 (2019).
23. A. Leonard, L. Ponson, C. Daraio, Wave mitigation in ordered networks of granular chains. *J. Mech. Phys. Solid.* **73**, 103–117 (2014).
24. X. Jia, C. Caroli, B. Velicky, Ultrasound propagation in externally stressed granular media. *Phys. Rev. Lett.* **82**, 1863–1866 (1999).
25. V. Langlois, X. Jia, Sound pulse broadening in stressed granular media. *Phys. Rev.* **91**, 022205 (2015).
26. C. Coste, B. Gilles, On the validity of hertz contact law for granular material acoustics. *Eur. Phys. J. B Condens. Matter Complex Syst.* **7**, 155–168 (1999).
27. E. T. Owens, K. E. Daniels, Sound propagation and force chains in granular materials. *Europhys. Lett.* **94**, 54005 (2011).
28. J. Goddard, Nonlinear elasticity and pressure-dependent wave speeds in granular media. *Proc. Roy. Soc. Lond. Math. Phys. Sci.* **430**, 105–131 (1990).
29. H. A. Makse, N. Gland, D. L. Johnson, L. Schwartz, Granular packings: Nonlinear elasticity, sound propagation, and collective relaxation dynamics. *Phys. Rev.* **70**, 061302 (2004).
30. B. O. Hardin, F. Richart Jr., Elastic wave velocities in granular soils. *J. Soil Mech. Found Div.* **89**, 33–65 (1963).
31. B. O. Hardin, W. L. Black, Sand stiffness under various triaxial stresses. *J. Soil Mech. Found Div.* **92**, 27–42 (1966).
32. M. A. Zimmer, M. Prasad, G. Mavko, A. Nur, Seismic velocities of unconsolidated sands. Part 1. Pressure trends from 0.1 to 20 mpa. *Geophysics* **72**, E1–E13 (2007).
33. A. Gheibi, A. Hedayat, Ultrasonic investigation of granular materials subjected to compression and crushing. *Ultrasonics* **87**, 112–125 (2018).
34. J. Santamarina, G. Cascante, Stress anisotropy and wave propagation: A micromechanical view. *Can. Geotech. J.* **33**, 770–782 (1996).
35. J. O'Donovan *et al.*, Micromechanics of seismic wave propagation in granular materials. *Granul. Matter* **18**, 56 (2016).
36. S. Van den Wildenberg, M. van Hecke, X. Jia, Evolution of granular packings by nonlinear acoustic waves. *Europhys. Lett.* **101**, 14004 (2013).
37. E. Somfai, J. N. Roux, J. H. Snoeijer, M. Van Hecke, W. Van Saarloos, Elastic wave propagation in confined granular systems. *Phys. Rev.* **72**, 021301 (2005).
38. A. Merkel, V. Tournat, V. Gusev, Experimental evidence of rotational elastic waves in granular phononic crystals. *Phys. Rev. Lett.* **107**, 225502 (2011).
39. A. H. Clark, L. Kondic, R. P. Behringer, Particle scale dynamics in granular impact. *Phys. Rev. Lett.* **109**, 238302 (2012).
40. R. K. Shrivastava, Effect of disorder on bulk sound wave speed: A multiscale spectral analysis. *Nonlinear Process Geophys.* **24**, 435–454 (2017).
41. R. F. Waymel, E. Wang, A. Awasthi, P. H. Geubelle, J. Lambros, Propagation and dissipation of elasto-plastic stress waves in two dimensional ordered granular media. *J. Mech. Phys. Solid.* **120**, 117–131 (2018).
42. T. Brunet, X. Jia, P. Mills, Mechanisms for acoustic absorption in dry and weakly wet granular media. *Phys. Rev. Lett.* **101**, 138001 (2008).
43. E. B. Herbold, V. F. Nesterenko, The role of dissipation on wave shape and attenuation in granular chains. *Phys. Procedia* **3**, 465–471 (2010).
44. D. O. Potyondy, P. Cundall, A bonded-particle model for rock. *Int. J. Rock Mech. Min. Sci.* **41**, 1329–1364 (2004).
45. A. Di Renzo, F. P. Di Maio, Comparison of contact-force models for the simulation of collisions in DEM-based granular flow codes. *Chem. Eng. Sci.* **59**, 525–541 (2004).
46. A. Di Renzo, F. P. Di Maio, An improved integral non-linear model for the contact of particles in distinct element simulations. *Chem. Eng. Sci.* **60**, 1303–1312 (2005).
47. D. L. Johnson, Y. Hu, H. Makse, Density of states in granular media in the presence of damping. *Phys. Rev.* **91**, 062208 (2015).
48. R. Hurley *et al.*, Linking initial microstructure and local response during quasistatic granular compaction. *Phys. Rev.* **96**, 012905 (2017).
49. H. A. Makse, D. L. Johnson, L. M. Schwartz, Packing of compressible granular materials. *Phys. Rev. Lett.* **84**, 4160–4163 (2000).
50. K. L. Johnson, K. L. Johnson, *Contact Mechanics* (Cambridge University Press, 1987).
51. K. J. Hanley, C. O'Sullivan, Analytical study of the accuracy of discrete element simulations. *Int. J. Numer. Methods Eng.* **109**, 29–51 (2017).
52. T. Caughey, M. E. O'Kelly, Classical normal modes in damped linear dynamic systems. *J. Appl. Mech.* **32**, 583–588 (1965).
53. D. Gorham, A. Kharaz, The measurement of particle rebound characteristics. *Powder Technol.* **112**, 193–202 (2000).
54. R. Hurley, S. Hall, J. Wright, Multi-scale mechanics of granular solids from grain-resolved x-ray measurements. *Proc. Math. Phys. Eng. Sci.* **473**, 20170491 (2017).
55. R. Hurley, J. Lind, D. Pagan, M. Akin, E. Herbold, In situ grain fracture mechanics during uniaxial compaction of granular solids. *J. Mech. Phys. Solid.* **112**, 273–290 (2018).
56. R. Hurley, E. Marteau, G. Ravichandran, J. E. Andrade, Extracting inter-particle forces in opaque granular materials: Beyond photoelasticity. *J. Mech. Phys. Solid.* **63**, 154–166 (2014).
57. R. Hurley, K. Lim, G. Ravichandran, J. Andrade, Dynamic inter-particle force inference in granular materials: Method and application. *Exp. Mech.* **56**, 217–229 (2016).
58. E. Oberg, F. D. Jones, H. L. Horton, H. H. Ryffel, J. H. Geronimo, *Machinery's Handbook* (Industrial Press, New York, 2004), vol. 200.
59. C. Sandeep, K. Senetakis, Grain-scale mechanics of quartz sand under normal and tangential loading. *Tribol. Int.* **117**, 261–271 (2018).
60. C. Zhai, E. B. Herbold, R. C. Hurley, Dataset for article titled "The influence of packing structure and interparticle forces on ultrasound transmission in granular media." Zenodo. https://zenodo.org/record/3785083. Deposited 18 May 2020.